

¹State Key Laboratory of Biochemical Engineering, Institute of Process

Engineering, Chinese Academy of Sciences, Beijing 100190, China;

²Department of Physical Chemistry, School of Metallurgical and Ecological Engineering,

University of Science and Technology Beijing, Beijing 100083, China;

³University of Chinese Academy of Sciences, Chinese Academy of Sciences, Beijing 100049, China;

⁴School of Materials Science and Engineering, Nanjing University of Posts and Telecommunications, Nanjing 210046,

China; ⁵School of Chemical Engineering and Australian Institute for Bioengineering and Nanotechnology, The University of Queensland, St Lucia 4072, Australia and

⁶Institute of Physics, Chinese Academy of Sciences, Beijing 100190, China

CHEMISTRY

Special Topic: Hierarchically Porous Materials

Efficient sequential harvesting of solar light by heterogeneous hollow shells with hierarchical pores

Yanze Wei^{1,2,†}, Jiawei Wan^{1,†}, Nailiang Yang^{1,3,†}, Yu Yang¹, Yanwen Ma⁴, Songcan Wang⁵, Jiangyan Wang^{1,‡}, Ranbo Yu², Lin Gu⁶, Lianhui Wang⁴, Lianzhou Wang⁵, Wei Huang^{4,*} and Dan Wang^{1,3,*}

ABSTRACT

In nature, sequential harvesting of light widely exists in the old life entity, i.e. cyanobacteria, to maximize the light absorption and enhance the photosynthesis efficiency. Inspired by nature, we propose a brand new concept of temporally-spatially sequential harvesting of light in one single particle, which has purpose-designed heterogeneous hollow multi-shelled structures (HoMSs) with porous shells composed of nanoparticle subunits. Structurally, HoMSs consist of different band-gap materials outside-in, thus realizing the efficient harvesting of light with different wavelengths. Moreover, introducing oxygen vacancies into each nanoparticle subunit can also enhance the light absorption. With the benefit of sequential harvesting of light in HoMSs, the quantum efficiency at wavelength of 400 nm is enhanced by six times compared with the corresponding nanoparticles. Impressively, using these aforementioned materials as photocatalysts, highly efficient photocatalytic water splitting is realized, which cannot be achieved by using the nanoparticle counterparts. This new concept of temporally-spatially sequential harvesting of solar light paves the way for solving the ever-growing energy demand.

Keywords: light harvesting, hollow structures, multi-shelled, solar energy conversion

INTRODUCTION

Solar energy conversion is an ideal path for addressing the global energy and environmental crisis [1–3]. Among the various steps of the solar energy conversion process, sunlight harvesting is the primary step, which determines the energy conversion efficiency [4–8]. Natural photosynthesis is the ultimate model for solar-to-chemical conversion, which provides the solution to enhancing sunlight harvesting efficiency [9–12]. In the antenna system of cyanobacteria, which represents the oldest life entity on our earth and accumulates large amounts of oxygen for oxygenic life, different antenna pigments are loaded in a certain order to realize the sequential collection of light energy (from the outside to the inside: phycoerythrin (570 nm), phycocyanin (630 nm), allophycocyanin (650 nm), chlorophyll α (670–678 nm)), thus reaching the maximum light absorption (Sup-

plementary Fig. 1). As a result, this structure ensures a fast and precise route to driving the redox reaction and completing the energy conversion process [13–15].

As reported, nature-inspired materials have been long desired by human society, as they generally possess unexpected properties and show great advantages in many fields [16–20]. To mimic the sequential light harvesting in the antenna system of cyanobacteria and realize efficient light utilization, the desired photosynthetic system should meet the following requirements from structure to function: (1) multi-shelled membrane system to confine the photosynthetic process; (2) sequential harvesting of light in antenna system (absorb the shorter wavelength outside, and absorb the longer wavelength inside) to improve light absorption efficiency; (3) porous shells on the membrane for mass

***Corresponding**

authors. E-mails: danwang@ipe.ac.cn; iamwhuang@nwpu.edu.cn

[†]Equally contributed to this work.

[‡]Present affiliation: Department of Materials Science and Engineering, Stanford University, Stanford, CA 94305, USA

Received 21

November 2019;

Revised 1 March

2020; **Accepted 27**

March 2020

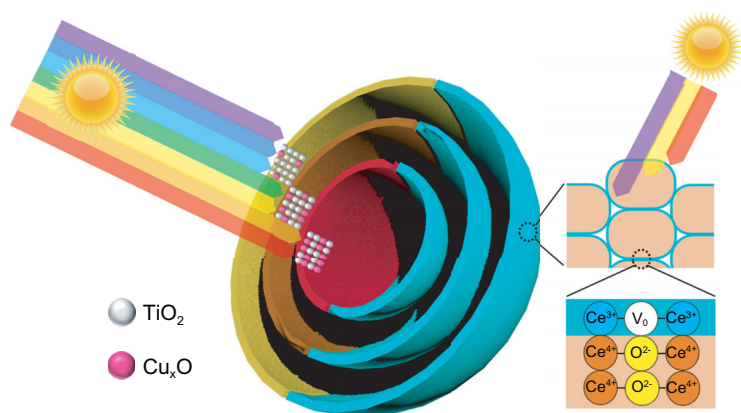


Figure 1. Illustration of two designed heterogeneous HoMSs for efficient sequential harvesting of solar light. The left part represents TCHoMSs, while the right part represents CFHoMSs. V_0 indicates oxygen vacancy. The left part of the scheme shows an increased molar ratio of Ti/Cu along outside-in $\text{TiO}_2\text{-Cu}_x\text{O}$ shells, which enables sequential harvesting of weakly penetrable short-wavelength light- by the outer part and strongly penetrable long-wavelength light- by the inner part. The different colors of the multiple shells indicate their different compositions. The right part of the scheme shows that abundant oxygen vacancies exist on the surface of $\text{CeO}_2\text{-CeFeO}_3$ nanoparticle subunits, thus realizing sequential light- harvesting from the surface to the inside of each nanoparticle subunit.

transfer; and (4) short route for fast charge transport [21–23].

Herein, inspired by the ingenious natural photosynthesis system, three-dimensional (3D) hollow multi-shelled structures (HoMSs) with porous shells composed of zero-dimensional (0D) nanoparticle subunits are constructed to establish the artificial photosynthesis system [24–26], which meets the aforementioned requirements as: (1) the size and the multiple shell structure of 3D HoMSs are proper to perform as nano-micro reactors; (2) most importantly, the sequential harvesting of sunlight in HoMSs is realized by introducing various materials with different band gaps into different shells. The temporal-spatial ordering of heterogeneous shells enables the weakly penetrable short-wavelength light and strongly penetrable long-wavelength light to be preferentially absorbed by the outer and inner part of HoMSs, respectively, thus greatly improving light absorption efficiency and ensuring dispersed excitation events on distinct shells. Furthermore, the sequential light harvesting can also be realized by introducing oxygen vacancies onto the surface of each 0D subunit, thus enhancing light utilization; (3) the porous shells are similar to the membrane system, which facilitates mass transfer; and (4) the thin shell of HoMSs could shorten the diffusion paths of photo-excited carriers [27–30]. Owing to the biomimetic structure and functions analogous to the antenna system of cyanobacteria, the 3D heterogeneous HoMSs system is highly

expected to show promising potential in realizing efficient artificial photoreaction [31].

As Fig. 1 shows, $\text{TiO}_2\text{-Cu}_x\text{O}$ hollow multi-shelled structures (TCHoMSs) and $\text{CeO}_2\text{-CeFeO}_3$ hollow multi-shelled structures (CFHoMSs) with different compositional nanoparticle subunits and shells were fabricated to realize sequential harvesting of solar light. For TCHoMSs, the outer part is mainly composed of broad-band-gap TiO_2 semiconductors (Ti/Cu = 15:1) that can absorb weakly penetrable short-wavelength light, while the inner part consists of increased ratio of narrow-band-gap Cu_xO semiconductors (Ti/Cu = 6:1) that can absorb strongly penetrable long-wavelength light. In addition, sequential light harvesting of each 0D subunit of the triple-shelled $\text{CeO}_2\text{-CeFeO}_3$ hollow structures (3S-CFHoMSs) was realized by introducing oxygen vacancies into the surface of each nanoparticle subunit. To experimentally prove the benefits of our newly proposed concept, photocatalytic water splitting was chosen as a model reaction, using purpose-designed heterogeneous HoMSs as photocatalysts. As a result, quadruple-shelled $\text{TiO}_2\text{-Cu}_x\text{O}$ hollow structures (4S-TCHoMSs) presented significantly enhanced hydrogen evolution activity and stability ($2490 \mu\text{mol/h}$, 90 h), compared to $\text{TiO}_2\text{-Cu}_x\text{O}$ nanoparticles or reversed $\text{TiO}_2\text{-Cu}_x\text{O}$ heterostructures. Excellent oxygen evolution rate ($452 \mu\text{mol/h}$) was also achieved by 3S-CFHoMSs, which greatly benefited from the surface oxygen vacancies and heterojunctions on each subunit. Owing to the enhanced light absorption, the overall water splitting based on particle suspension system was achieved by combining 4S-TCHoMSs and 3S-CFHoMSs with the aid of redox shuttle.

Synthesis and characterization of two heterogeneous HoMSs

The accurate synthesis of HoMSs remains a challenge, especially for obtaining distinct compositions within different shells to realize sequential light- harvesting [32]. Herein, $\text{TiO}_2\text{-Cu}_x\text{O}$ hollow multi-shelled structures with tunable shell number (single-, double-, triple- and quadruple-shelled) and different inner/outer shell composition were synthesized through a sequential template method by accurately controlling the cation absorption process of carbon microsphere (CMS) templates. By adjusting ion concentrations, ion radius and ion charges, the distribution and amount of adsorbed precursors in CMS templates can be well controlled, thus the shell composition can be purposely tuned [33–36]. On one hand, the Ti precursor concentration is much higher than Cu precursor

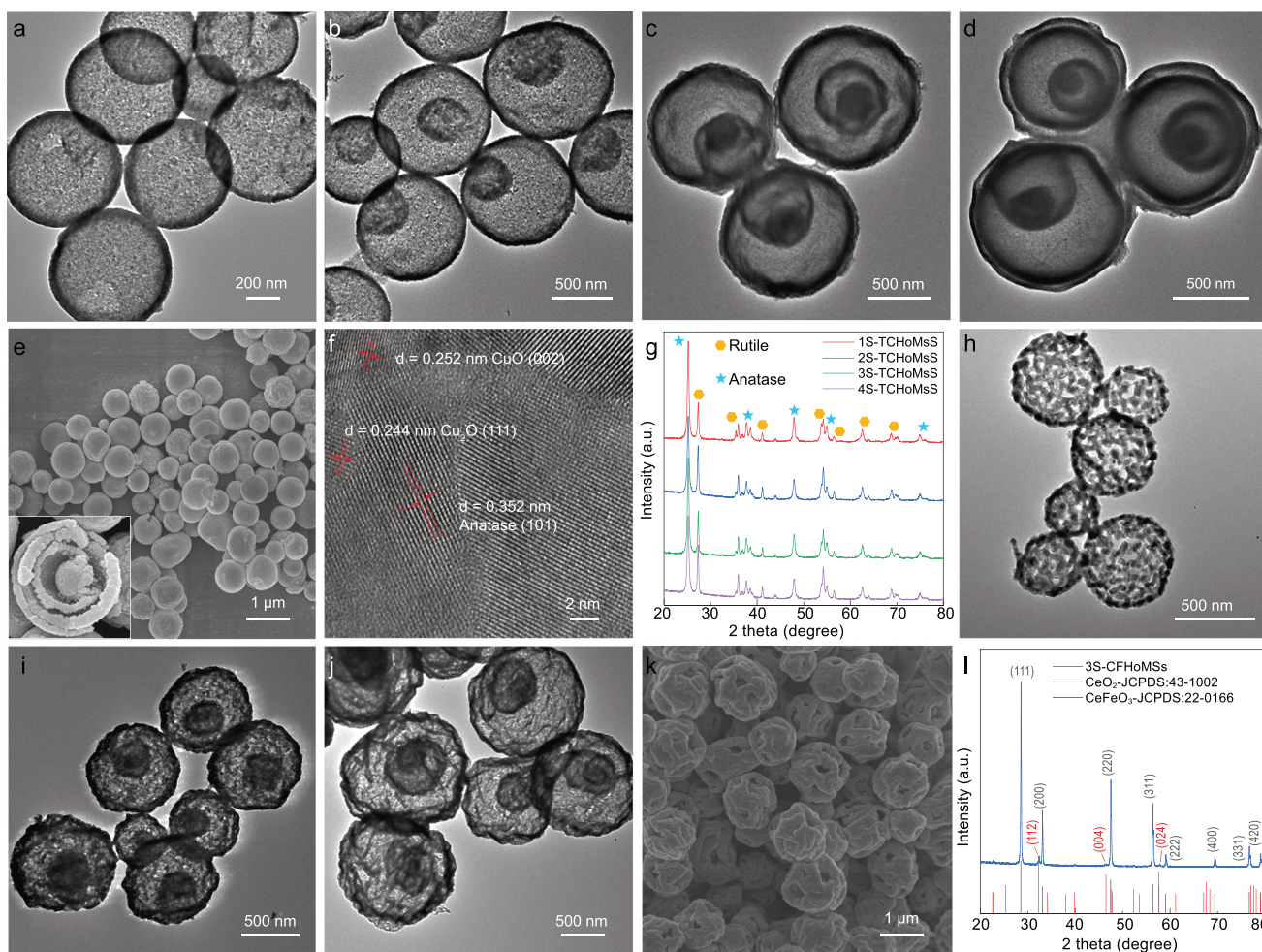


Figure 2. Morphological and structural analysis of as-prepared HoMSs. (a–d) TEM images and (e) SEM image of TCHoMSs: (a) single-shelled (1S-), (b) double-shelled (2S-), (c) triple-shelled (3S-) and (d, e) quadruple-shelled (4S-) TCHoMSs (inset is the high-magnification SEM image of one typical microsphere); (f) HRTEM image of TCHoMSs; (g) XRD patterns of TCHoMS samples; (h–j) TEM images of CeO_2 - CeFeO_3 CFHoMSs: (h) single-shelled (1S-), (i) double-shelled (2S-) and (j) triple-shelled (3S-) CFHoMSs; (k) SEM image of 3S-CFHoMSs; (l) XRD pattern of 3S-CFHoMSs.

concentration, leading to a higher overall ratio of Ti in the TiO_2 - Cu_xO products. On the other hand, $[\text{Cu}(\text{H}_2\text{O})_4]^{2+}$ cation has a smaller hydrated ionic radius and is more positively charged than Ti coordination cations $[\text{Ti}(\text{OH})_n(\text{H}_2\text{O})_{6-n}]^{(4-n)+}$ ($n = 2, 3$), thus $[\text{Cu}(\text{H}_2\text{O})_4]^{2+}$ cations can be more easily adsorbed into the center of CMS, resulting in a molar ratio gradient of Ti/Cu [37,38]. After removing the CMS templates through a combustion process, TCHoMSs with different shell compositions are fabricated. Besides, increase of adsorption temperature and duration can improve the absorption depth and amount of precursors, thus increasing the shell number of hollow structures.

Scanning electron microscopy (SEM) images illustrate the uniform spherical morphology of TCHoMSs with a size around 600–800 nm (Fig. 2a–d), of which the inner hierarchical structure is clearly shown in the inserted image (Fig. 2e).

Transmission electron microscopy (TEM) images show that the shells are composed of tiny crystal grains (size: ~ 17.6 nm, similar to ~ 15.8 nm derived from X-ray diffraction (XRD) calculation), and the thicknesses of shells range from 34 to 62 nm (Supplementary Fig. 2). Besides, the lattice spacings of 0.352 and 0.325 nm correspond to anatase (101) plane and rutile (110) plane, respectively, indicating that different TiO_2 phases exist in the sample, while the observed lattice spacings of 0.252 nm for CuO (002) plane and 0.244 nm for Cu_2O (111) plane prove that the Cu_xO phases are attached tightly to the TiO_2 particles (Fig. 2f). As shown in XRD patterns (Fig. 2g), the main peaks of samples with different numbers of shells are indexed to TiO_2 (anatase: JCPDS card no. 21–1272 and rutile: JCPDS card no. 21–1276). Although the peaks of copper oxides are not observed in the XRD patterns, which is possibly due to the low concentration of Cu_xO in the

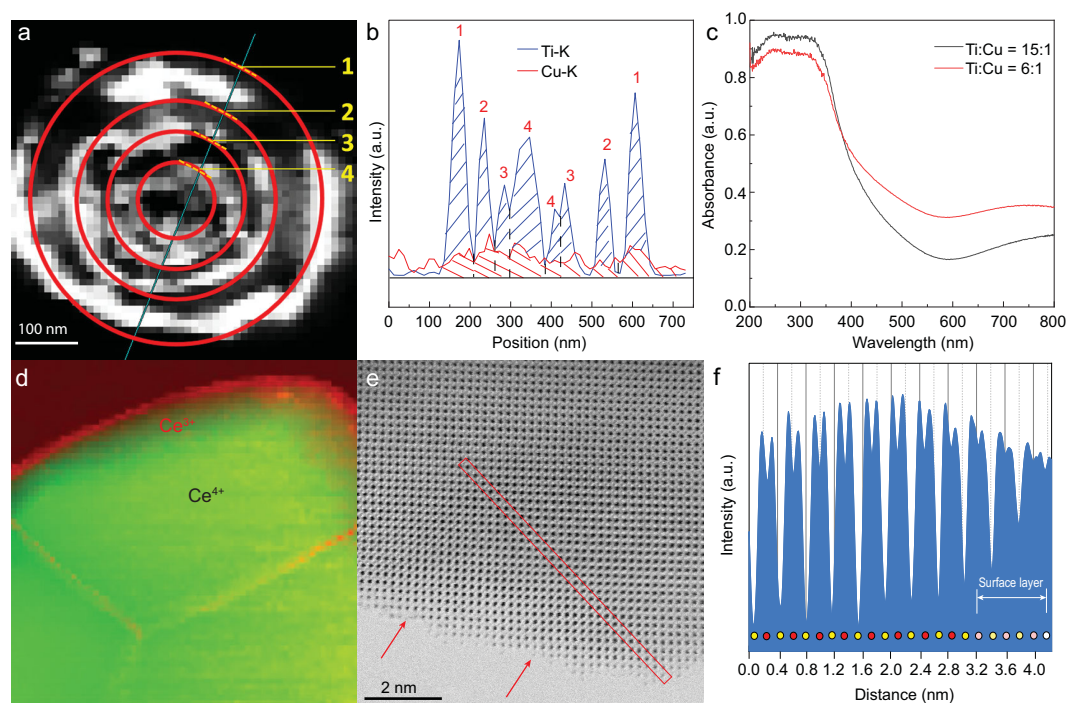


Figure 3. Structural characterization and sequential light absorption of TCHoMSs and CFHoMSs. (a) Dark-field TEM image of a slice of 4S-TCHoMSs; (b) EDS line scanning along the cyan line in (a), showing the Ti/Cu ratios in different shells; (c) absorption spectrum of $\text{TiO}_2\text{-Cu}_x\text{O}$ single-shelled hollow structures with Ti/Cu molar ratio of 15:1 and 6:1; (d) EELS mapping of Ce^{3+} and Ce^{4+} , showing their distribution in the crystals (green: Ce^{4+} ; red: Ce^{3+}); (e) the spherical aberration-corrected STEM image of 3S-CFHoMSs (the single crystal surface, with red arrows indicating the atom steps); (f) the corresponding line profile of the area in the red rectangle in (e) with the direction from the upper left to the bottom right.

material being below the detection limit of XRD, the Cu 2p peak located at 935 eV in X-ray photoelectron spectroscopy (XPS) spectrum of TCHoMSs confirmed the existence of Cu element (Supplementary Fig. 3a).

Further information from high-resolution XPS spectra of Cu 2p orbital indicates that Cu element is mainly composed of Cu (I) and Cu (II) with a molar ratio of 6:5 (Supplementary Fig. 3b). Similar Cu (I) and Cu (II) ratio was observed for the $\text{TiO}_2\text{-Cu}_x\text{O}$ nanoparticles (Supplementary Fig. 3c). Comparing the laser Raman spectra of pure TiO_2 and 4S-TCHoMSs, no peak shifts were observed, which confirmed that no Cu doping was detected (Supplementary Fig. 3d).

Furthermore, $\text{CeO}_2\text{-CeFeO}_3$ HoMSs were prepared through a similar sequential template method to realize the sequential light harvesting of each 0D nanoparticle subunit of the 3D HoMSs. After a specific calcination process, single-, double- and triple-shelled $\text{CeO}_2\text{-CeFeO}_3$ hollow structures with big pores on the surface are obtained, as shown by TEM images (Fig. 2h–j). SEM image illustrates the porous surface more clearly, where small crystals sintered together to form the shells as well as create big holes in the shells (Fig. 2k). XRD pattern of the triple-

shelled sample shows that the main peaks are indexed to CeO_2 phase (JCPDS card no. 43–1002) and CeFeO_3 phase (JCPDS card no. 22–0166) (Fig. 2l).

Sequential absorption of light in as-prepared HoMSs

To qualitatively study the relative molar ratio of Ti/Cu in different shells, 4S-TCHoMSs slices with a thickness around 40 nm were obtained with the aid of resin embedding agent (Fig. 3a). The molar ratio of Ti/Cu is estimated by energy dispersive X-ray spectroscopy (EDS). The Ti/Cu ratio in the outermost shell is around 15:1, while the inner shells have an increased Cu content, which has a Ti/Cu ratio of approximately 6:1 (Fig. 3b). To further analyse the absorption spectrum of different layers of 4S-TCHoMSs, $\text{TiO}_2\text{-Cu}_x\text{O}$ single-shelled hollow structures with two different Ti/Cu molar ratios of 15:1 and 6:1 are synthesized through the similar sequential template approach. The Ti/Cu ratio is further confirmed by inductively coupled plasma mass spectrometry (ICP-MS) (Supplementary Tables 1 and 2). As illustrated in Fig. 3c, the hollow spheres with Ti/Cu ratio of 15:1 show

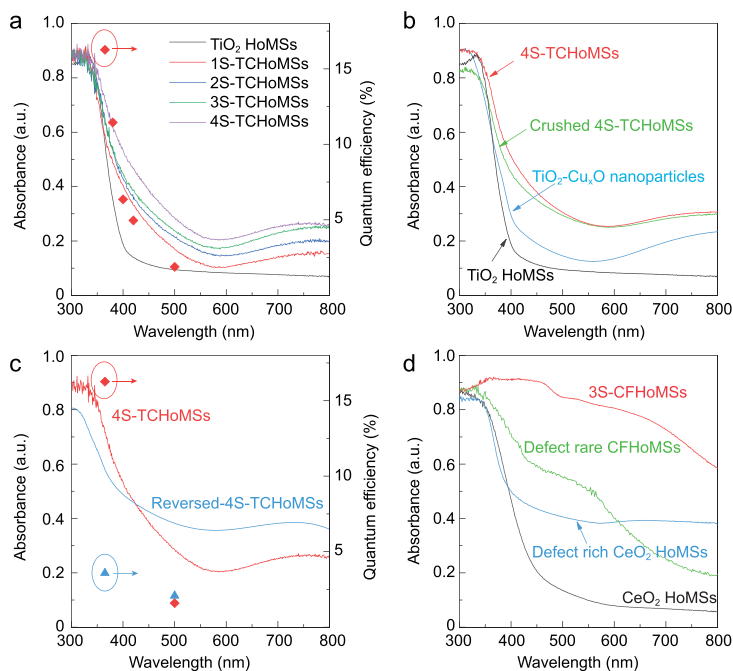


Figure 4. Sequential light absorption properties of HoMSs. (a) UV-Vis absorption curves of TCHoMSs with different shell numbers and apparent quantum efficiency (red diamonds) of 4S-TCHoMSs at different wavelengths; (b) UV-Vis absorption curves of 4S-TCHoMSs $\text{TiO}_2\text{-Cu}_x\text{O}$ nanoparticles, crushed 4S-TCHoMSs and TiO_2 HoMSs; (c) UV-Vis absorption curves and apparent quantum efficiency of 4S-TCHoMSs (red diamonds) and reversed 4S-TCHoMSs (blue triangles); (d) UV-Vis absorption curves of 3S-CFHoMSs, CeO_2 HoMSs and the corresponding samples with surface defect control.

higher ultraviolet (UV) light absorbance due to the higher portion of TiO_2 composition, indicating that UV light can be better absorbed by the outermost shell of 4S-TCHoMSs. In comparison, a conspicuous increase of absorption in the spectrum of 400–600 nm is achieved for the hollow structures with Ti/Cu ratio of 6:1. The result indicates that inner shells of 4S-TCHoMSs have better response to visible light (Supplementary Fig. 4). As it is acknowledged, diffraction ability of light is enhanced with the increase of wavelength [39,40]. Visible light is more likely to diffract through the porous shell and be absorbed by the inner shells, while the short-wavelength UV light is more easily directly absorbed by the outer shells. As a result, by deliberately developing a ratio gradient of Ti/Cu along the shells, sequential absorption of sunlight is achieved in a sequence from UV light to visible light.

In addition to the chemical composition of shells, the light-harvesting ability is also related to the number of shells and the unique hollow structure. The ultraviolet-visible (UV-Vis) absorption curves demonstrate that the entire light absorption increases with the increase of shell number (Fig. 4a). Notably, with the introduction

of space sequential light-harvesting structures, the 4S-TCHoMSs exhibited the highest absorption in visible light region. Moreover, to quantify the spectral distribution of the photocatalytic activity of 4S-TCHoMSs, the apparent quantum efficiency (AQE) for hydrogen evolution reaction (HER) was measured at single wavelength of 365, 400, 420 and 500 nm. The AQE decreases obviously with increasing wavelength, and the detectable efficiency calculated at 500 nm indicates that the existence of Cu_xO enables the UV responsive TiO_2 to carry on HER reaction within visible light region. The enhancement in light-harvesting ability could be further observed by comparing the UV-Vis spectra of TCHoMSs with those of $\text{TiO}_2\text{-Cu}_x\text{O}$ nanoparticles (TCNPs), TiO_2 HoMSs and the corresponding crushed 4S-HoMSs (Fig. 4b). The collapse of the highly ordered structures greatly influenced light scattering and reduced light absorption in a broad wavelength (Supplementary Fig. 5). Interestingly, although the inner shells had more Cu_xO content exposed after the HoMSs were crushed, the light absorption in visible light region still showed a slight decrease. In addition, 4S-TCHoMSs with reversed TiO_2 and Cu_xO compositions were synthesized to demonstrate the importance of light-harvesting sequence (Supplementary Fig. 6). Owing to higher Cu_xO content in the outer shells, the reversed 4S-TCHoMSs showed enhanced visible light absorption, but the UV absorption was greatly hindered (Fig. 4c), which was also conspicuously reflected by the different AQE of HER (Fig. 4c).

Additionally, we intentionally designed CFHoMSs, in which oxygen vacancies exist on the surface of each 0D nanoparticle subunit for efficient harvesting of solar light. The surface of a single crystal is highlighted in the high-resolution spherical aberration-corrected scanning transmission electron microscopy (STEM) image (Fig. 3e). Atomic steps are visibly presented and marked with red arrows, indicating the atom absence at the surface. The inter-atomic distance obtained by line profiles along the red section shows that the oxygen vacancies are mainly distributed at the surface area of the grains [41]. Besides, electron energy loss spectroscopy (EELS) demonstrates that Ce^{3+} mainly concentrates at the outer surface with a thickness around 3.3 nm, indicating that surface defects locate at the edge of the crystals and grain boundaries [42] (Fig. 3d, red edge), while the body part of the crystalline grain is CeO_2 (Fig. 3d, green part). The increased Ce^{3+} portion and oxygen vacancies are also confirmed by the high-resolution XPS spectra of Ce 3d and O 1s orbits. After the treatment in reductive atmosphere, the peaks attributed to Ce^{3+} and the chemisorbed peroxide oxygen

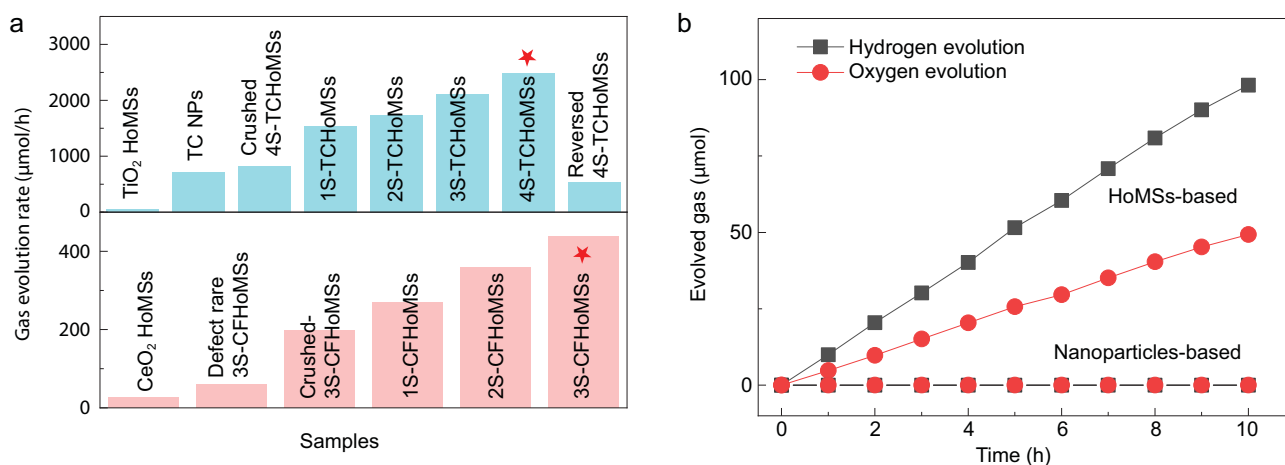


Figure 5. Water splitting performance of TCHoMSs and CFHoMSs. (a) Hydrogen evolution activity and oxygen evolution activity of TCHoMSs and CFHoMSs related samples under 300 W Xe lamp irradiation at 281 K; (b) the overall water splitting performance of 4S-TCHoMSs and CFHoMSs under 300 W Xe lamp irradiation at 281 K.

(O_2^{2-}), which acts as the active oxygen, increased remarkably [43] (Supplementary Fig. 7a and b). As described in previous experimental and theoretical studies, these oxygen vacancies function as active centers for gas evolution reaction, and water molecules are inclined to be adsorbed by the Ce^{3+} ions or oxygen vacancies, which reduce the energy barrier of water oxidation [43,44]. Owing to the surface oxygen vacancies and CeFeO_3 phase, these CFHoMSs exhibited an enhanced light absorption with a broader absorption edge of visible light as illustrated in Fig. 4b. The creation of surface oxygen vacancies and combination with CeFeO_3 significantly increased the light absorption of each subunit of CFHoMSs. The effect of surface oxygen vacancies in light absorption could be testified by comparing the UV-Vis spectra of CFHoMSs and CFHoMSs after oxygen treatment at 800°C . 3S-CFHoMSs exhibited the highest light absorption both in the UV and visible region, much stronger than CeO_2 HoMSs with surface oxygen vacancies and CeO_2 - CeFeO_3 without surface oxygen vacancies. As expected, the 3S-CFHoMS sample, which has the highest shell number, showed the best light absorption ability as well as the lowest photoluminescence intensity (Supplementary Fig. 7c and d).

Water splitting performance

To prove the concept of sequential light harvesting, we chose photocatalytic water splitting as a model reaction. TCHoMSs display excellent hydrogen evolution rate under 300 W Xe lamp irradiation in the solution of methanol and deionized water. The linear hydrogen evolution curves of TCHoMSs (Supplementary Fig. 8a)

indicate the stable reaction within six hours. As expected, all the TCHoMSs showed better HER properties than the TCNPs with the same content. As shell number increases, the enhanced hydrogen evolution performance of TCHoMSs further confirmed the benefit from the sequential light-harvesting design [45]. Impressively, 4S-TCHoMSs exhibited the best performance with a hydrogen evolution rate of $2490 \mu\text{mol/h}$ (Fig. 5a). Importantly, more than 95% of the original activity after 16 cycles (96 hours) remained for 4S-TCHoMSs, which benefited from the inhibited photocorrosion due to the suppressed charge carrier accumulation [46], and the impressive structural stability of the HoMSs attributed to the multiple shells supporting each other and the exterior shell protecting the interior shells (Supplementary Fig. 8c).

Furthermore, to evaluate practical application feasibility of the photocatalyst, the performance of the as-synthesized samples under simulated sunlight with AM 1.5 G illumination is also measured (Supplementary Fig. 9). Impressively, owing to the introduction of Cu_xO and a fine sequential absorption structure, the 4S-TCHoMSs exhibited the best performance ($320 \mu\text{mol/h}$) among the TCHoMSs and considerably surpassed both TCNPs and TiO_2 HoMSs. The hydrogen evolution activity and stability of as-prepared 4S-TCHoMSs are the best among the reported TiO_2 -based materials (Supplementary Table 4). The band structure of TCHoMSs was confirmed by UV-Vis spectra and Mott-shcottonky measurements, as illustrated in Supplementary Fig. 10. In addition, the electron transport paths between TiO_2 and Cu_xO were revealed by photocurrent responses under different incident light wavelength (Supplementary Fig. 11) [47].

The importance of sequential light harvesting on the selected 4S-TCHoMSs in the application of photocatalytic HER was also verified by TCHoMSs with reversed TiO_2 and Cu_xO compositions. Owing to the increased content of Cu, although slight increase of visible light driven photocatalytic HER performance was observed, the performance under Xe lamp irradiation decreased to almost one-fifth of the 4S-TCHoMSs (Supplementary Fig. 6c). The different HER performance verified that sequential light harvesting is significant for light utilization in HoMSs, as nature shows us.

As the other half reaction of overall solar water splitting, the four-electron oxygen evolution reaction (OER) with higher reaction barriers is more difficult to realize than HER. The photocatalytic water oxidation performance of CFHoMSs was evaluated using 0.01 M AgNO_3 as the sacrificial agent under the same 300 W Xe lamp irradiation. As shown in Fig. 5a, among the CeO_2 - CeFeO_3 related samples, the maximum O_2 evolution rate of $452 \mu\text{mol/h}$ was achieved by 3S-CFHoMSs, which also processes the highest light absorption ability (Supplementary Fig. 8b). We further checked the photocatalytic durability of the corresponding samples by the repeated purge and injection cycles with an interval of two hours. As shown in Supplementary Fig. 8d, the O_2 evolution rates of all these samples show gradual decrease, and the overall durability of the most active sample 3S-CFHoMSs is less than five hours. Nevertheless, both the oxygen evolution rate and stability of our photocatalyst are outstanding among transition metal oxide- and ceria-based photocatalyst materials (Supplementary Table 5).

The evolution of H_2 and O_2 from 100 mL water with the aid of redox shuttle under Xe lamp irradiation is shown in Fig. 5b, in which the calculated H_2 and O_2 production in 10 hours is ~ 98 and $\sim 46 \mu\text{mol}$, respectively. Activity under simulated sunlight irradiation was also confirmed in Supplementary Fig. 12. Impressively, no production was detected using TiO_2 - Cu_xO and defect rare CeO_2 - CeFeO_3 nanoparticles, but H_2 and O_2 were continuously evolved in the HoMSs system under the same reaction condition, which is attributed to the structure design. The hollow multi-shell structures greatly increased the light-harvesting ability of photocatalysts, and we believe the charge transportation and surface properties improved by introducing HoMSs into the photocatalytic system also significantly drove the reaction. The comparison of both XPS spectra of Cu 2p for TCHoMSs and Ce 3d for CFHoMSs before and after the overall water splitting reaction have confirmed that the chemical com-

position remained stable during the photocatalytic reaction (Supplementary Fig. 13).

DISCUSSION

As confirmed by the characterizations, the design and synthesis of heterostructural HoMSs with the ability of sequential harvesting of light were realized for the first time. The aforementioned experimental results clearly indicate that 4S-TCHoMSs and 3S-CFHoMSs exhibit impressive enhanced light-harvesting ability. Choosing water splitting as a model reaction, the perfectly designed HoMSs can significantly improve the light utilization and bring a great enhancement in catalytic performance.

First, our new concept of sequential absorption of light from outer shell to the inner shells and from the outer part of individual nanoparticle subunit to its inner part, can efficiently improve light absorption, reduce light-to-heat conversion and decrease charge carrier recombination, thus significantly improving light conversion efficiency. The outside-in gradually increased Cu/Ti ratio on the shells enables the sequential absorption of weakly penetrable short-wavelength light by the outer shell and strongly penetrable long-wavelength light by the inner shells, thus widening the light absorption spectrum and strengthening the light absorption ability. The oxygen vacancies and CeFeO_3 mainly exist on the surface of CFHoMSs, which enable each nanoparticle subunit to sequentially harvest light from the edge to the inside, thus rendering CFHoMSs with visible light response and broadening the action spectrum.

Second, the enhanced photocatalytic water splitting performance was achieved by 4S-TCHoMSs and 3S-CFHoMSs with enhanced sequential light-harvesting ability and additional structural advantages: (1) thin shells shorten the diffusion paths of photogenerated carriers and facilitate electron-hole separation (Supplementary Fig. 14); (2) the aerophobic surface of the hollow structures favors the water absorption and gas desorption, thus improving the kinetic rate of the surface reaction (Supplementary Fig. 15); and (3) a heterostructure of TiO_2 and Cu_xO with the unique feature is created (0D nanoparticles make up 3D shells and support each other to construct 3D hollow structures) and greatly lowers both the interfacial and bulk charge-transfer resistance (Supplementary Fig. 16).

CONCLUSION

In summary, inspired by nature, by simulating the structure and function of cyanobacteria, the

sequential harvesting of solar light was successfully realized by well-designed heterogeneous HoMSs with distinct shells composed of different valance-state particles, paving a new route to enhancing light-harvesting efficiency. More impressively, the multiple merits of sequential light harvesting, including enhanced light absorption and inhibited charge carrier recombination, were experimentally verified by a model reaction of water splitting photocatalyzed by purpose-designed heterogeneous HoMSs: 4S-TCHoMSs achieved excellent HER activity of 2490 $\mu\text{mol/h}$, while 3S-CFHoMSs exhibited impressive OER activity of 452 $\mu\text{mol/h}$, which are among the best reported so far. This new wisdom of sequential harvesting of solar light or other electromagnetic waves with heterogeneous HoMSs may pave a new way for promoting the development in all photo-related fields as well as microwave absorption areas.

SUPPLEMENTARY DATA

Supplementary data are available at [NSR](#) online.

FUNDING

This work was supported by the National Natural Science Foundation of China (21590795, 21401199, 51472025, 21671016, 51872024, 21820102002 and 51802306), the National Key Research and Development Program of China (2016YFB0600903), the Scientific Instrument Developing Project of the Chinese Academy of Sciences (YZ201623), and the Queensland-Chinese Academy of Sciences Collaborative Science Fund (122111KYSB20170001).

AUTHOR CONTRIBUTIONS

D.W. and W.H. conceived the idea and supervised the research. Under the instruction of D.W. and R.Y., Y.W. and Y.Y. designed and performed the experiments. L.W. and S.W. confirmed the photocatalysis performance. L.G. characterized the high-angle annular dark-field and EELS images of CFHoMS. D.W., J.W., N.Y., J.W., Y.W., Y.Y., R.Y., L.W., Y.M., L.W. and W.H. analysed and discussed the experimental data and drafted the manuscript.

Conflict of interest statement. None declared.

REFERENCES

1. Gu JJ, Zhang W and Su HL *et al.* Morphology genetic materials templated from natural species. *Adv Mater* 2015; **27**: 464–78.
2. Graetzel M, Janssen RAJ and Mitzi DB *et al.* Materials interface engineering for solution-processed photovoltaics. *Nature* 2012; **488**: 304–12.
3. Gray HB. Powering the planet with solar fuel. *Nat Chem* 2009; **1**: 7.
4. Serpone N, Emeline AV and Ryabchuk VK *et al.* Why do hydrogen and oxygen yields from semiconductor-based photocat-

alyzed water splitting remain disappointingly low? Intrinsic and extrinsic factors impacting surface redox reactions. *ACS Energy Lett* 2016; **1**: 931–48.

5. Liu S, Tang ZR and Sun Y *et al.* One-dimension-based spatially ordered architectures for solar energy conversion. *Chem Soc Rev* 2015; **44**: 5053–75.
6. Kudo A and Miseki Y. Heterogeneous photocatalyst materials for water splitting. *Chem Soc Rev* 2009; **38**: 253–78.
7. Moniz SJA, Shevlin SA and Martin DJ *et al.* Visible-light driven heterojunction photocatalysts for water splitting—a critical review. *Energy Environ Sci* 2015; **8**: 731–59.
8. Manzi A, Tong Y and Feucht J *et al.* Resonantly enhanced multiple exciton generation through below-band-gap multi-photon absorption in perovskite nanocrystals. *Nat Commun* 2018; **9**: 1518.
9. Zhang BB and Sun LC. Artificial photosynthesis: opportunities and challenges of molecular catalysts. *Chem Soc Rev* 2019; **48**: 2216–64.
10. Kim W, Edri E and Frei H. Hierarchical inorganic assemblies for artificial photosynthesis. *Acc Chem Res* 2016; **49**: 1634–45.
11. Kornienko N, Zhang JZ and Sakimoto KK *et al.* Interfacing nature's catalytic machinery with synthetic materials for semi-artificial photosynthesis. *Nat Nanotechnol* 2018; **13**: 890–9.
12. Gust D, Moore TA and Moore AL. Solar fuels via artificial photosynthesis. *Acc Chem Res* 2009; **42**: 1890–8.
13. Tachibana Y, Vayssieres L and Durrant JR. Artificial photosynthesis for solar water-splitting. *Nat Photon* 2012; **6**: 511–8.
14. Li XB, Tung CH and Wu LZ. Semiconducting quantum dots for artificial photosynthesis. *Nat Rev Chem* 2018; **2**: 160–73.
15. Barber J. Photosynthetic energy conversion: natural and artificial. *Chem Soc Rev* 2009; **38**: 185–96.
16. Mao LB, Gao HL and Yao HB *et al.* Synthetic nacre by pre-designed matrix-directed mineralization. *Science* 2016; **354**: 107–10.
17. Liu M, Wang S and Jiang L. Nature-inspired superwettability systems. *Nat Rev Mater* 2017; **2**: 17036.
18. Zhang H, Liu H and Tian ZQ *et al.* Bacteria photosensitized by intracellular gold nanoclusters for solar fuel production. *Nat Nanotechnol* 2018; **13**: 900–5.
19. Zheng YM, Bai H and Huang ZB *et al.* Directional water collection on wetted spider silk. *Nature* 2010; **463**: 640–3.
20. Gao XF and Jiang L. Water-repellent legs of water striders. *Nature* 2004; **432**: 36.
21. Yang XG and Wang DW. Photocatalysis: from fundamental principles to materials and applications. *ACS Appl Energy Mater* 2018; **1**: 6657–93.
22. Wang YO, Suzuki H and Xie JJ *et al.* Mimicking natural photosynthesis: solar to renewable H₂ fuel synthesis by Z-scheme water splitting systems. *Chem Rev* 2018; **118**: 5201–41.
23. Yamamoto Y, Takeda H and Yui T *et al.* Efficient light harvesting via sequential two-step energy accumulation using a Ru-Re₅ multinuclear complex incorporated into periodic mesoporous organosilica. *Chem Sci* 2014; **5**: 639–48.
24. Wang JY, Tang HJ and Zhang LJ *et al.* Multi-shelled metal oxides prepared via an anion-adsorption mechanism for lithium-ion batteries. *Nat Energy* 2016; **1**: 16050.

25. Qi J, Zhao K and Li GD *et al.* Multi-shelled CeO₂ hollow microspheres as superior photocatalysts for water oxidation. *Nanoscale* 2014; **6**: 4072–7.
26. Mao D, Wan JW and Wang JY *et al.* Sequential templating approach: a ground-breaking strategy to create hollow multishelled structures. *Adv Mater* 2019; **31**: 1802874.
27. Yu A, Gentle I and Lu GQ *et al.* Nanoassembly of biocompatible microcapsules for urease encapsulation and their use as biomimetic reactors. *Chem Commun* 2006; **20**: 2150–2.
28. Wang JY, Wan JW and Wang D. Hollow Multishelled structures for promising applications: understanding the structure-performance correlation. *Acc Chem Res* 2019; **52**: 2169–78.
29. Wei YZ, Wang JY and Yu RB *et al.* Constructing SrTiO₃-TiO₂ heterogeneous hollow multi-shelled structures for enhanced solar water splitting. *Angew Chem Int Ed* 2019; **58**: 1422–6.
30. Wu X, Lu GQ and Wang LZ. Shell-in-shell TiO₂ hollow spheres synthesized by one-pot hydrothermal method for dye-sensitized solar cell application. *Energy Environ Sci* 2011; **4**: 3565–72.
31. Wang JY, Wan JW and Yang NL *et al.* Hollow multishell structures exercise temporal-spatial ordering and dynamic smart behaviour. *Nat Rev Chem* 2020; **4**: 159–68.
32. Qi J, Lai XY and Wang JY *et al.* Multi-shelled hollow micro-/nanostructures. *Chem Soc Rev* 2015; **44**: 6749–73.
33. Wang JY, Yang NL and Tang HJ *et al.* Accurate control of multishelled Co₃O₄ hollow microspheres as high-performance anode materials in lithium-ion batteries. *Angew Chem Int Ed* 2013; **52**: 6417–20.
34. Wang JY, Tang HJ and Wang H *et al.* Multi-shelled hollow micro-/nanostructures: promising platforms for lithium-ion batteries. *Mater Chem Front* 2017; **1**: 414–30.
35. Ren H, Yu RB and Wang JY *et al.* Muftishelled TiO₂ hollow microspheres as anodes with superior reversible capacity for lithium ion batteries. *Nano Lett* 2014; **14**: 6679–84.
36. Zhou L, Zhuang ZC and Zhao HH *et al.* Intricate hollow structures: controlled synthesis and applications in energy storage and conversion. *Adv Mater* 2017; **29**: 1602914.
37. Nightingale ER. Phenomenological theory of ion solvation-effective radii of hydrated ions. *J Phys Chem* 1959; **63**: 1381–7.
38. Hildenbrand VD, Fuess H and Pfaff G *et al.* Structural investigations on TiCl₄ solutions. *Z Phys Chem* 1996; **194**: 139–50.
39. National Aeronautics and Space Administration. *Optics: Light, Color, and Their Uses. An Educator's Guide with Activities in Science and Mathematics*. Washington, DC: Education Resources Information Center, 2000.
40. Bethe HA. Theory of diffraction by small holes. *Phys Rev* 1994; **66**: 163–82.
41. Lei WY, Zhang TT and Gu L *et al.* Surface-structure sensitivity of CeO₂ nanocrystals in photocatalysis and enhancing the reactivity with nanogold. *ACS Catal* 2015; **5**: 4385–93.
42. Turner S, Lazar S and Freitag B *et al.* High resolution mapping of surface reduction in ceria nanoparticles. *Nanoscale* 2011; **3**: 3385–90.
43. Zhao K, Qi J and Yin HJ *et al.* Efficient water oxidation under visible light by tuning surface defects on ceria nanorods. *J Mater Chem A* 2015; **3**: 20465–70.
44. Jiang D, Wang WZ and Zhang L *et al.* Insights into the surface-defect dependence of photoreactivity over CeO₂ nanocrystals with well-defined crystal facets. *ACS Catal* 2015; **5**: 4851–8.
45. Moon GD, Joo JB and Lee I *et al.* Decoration of size-tunable CuO nanodots on TiO₂ nanocrystals for noble metal-free photocatalytic H₂ production. *Nanoscale* 2014; **6**: 12002–8.
46. Toe CY, Zheng ZK and Wu H *et al.* Photocorrosion of cuprous oxide in hydrogen production: rationalising self-oxidation or self-reduction. *Angew Chem* 2018; **130**: 13801–5.
47. Chen HJ, Wang Q and Lyu MQ *et al.* Wavelength-switchable photocurrent in a hybrid TiO₂-Ag nanocluster photoelectrode. *Chem Commun* 2015; **51**: 12072–5.